



Article

Nano Application of Oil Concentration Detection Using Double-Tooth Ring Plasma Sensing

Lei Li ^{1,2}, Shubin Yan ^{2,3,*} , Yang Cui ^{2,3}, Chuanhui Zhu ^{2,3} , Taiquan Wu ^{2,3}, Qizhi Zhang ¹ and Guowang Gao ¹

¹ School of Electrical Engineering, Xi'an Shiyou University, Xi'an 710065, China; eleven_10086@163.com (L.L.); zhangqz@xsyu.edu.cn (Q.Z.); wwgao1205@163.com (G.G.)

² Zhejiang-Belarus Joint Laboratory of Intelligent Equipment and System for Water Conservancy and Hydropower Safety Monitoring, Hangzhou 310018, China; cuiy@zjweu.edu.cn (Y.C.); zhchh@zjweu.edu.cn (C.Z.); wutq@zjweu.edu.cn (T.W.)

³ School of Electrical Engineering, Zhejiang University of Water Resources and Electric Power, Hangzhou 310018, China

* Correspondence: yanshb@zjweu.edu.cn; Tel.: +86-186-3611-2255

Abstract: Based on the unique properties of optical Fano resonance and plasmonic-waveguide coupling systems, this paper explores a novel refractive index concentration sensor structure. The sensor structure is composed of a metal–insulator–metal (MIM) waveguide and two identically shaped and sized double-tooth ring couplers (DTR). The performance structure of the nanoscale refractive index sensor with DTR cavity was comprehensively assessed using the finite element method (FEM). Due to the impact of various geometric parameters on the sensing characteristics, including the rotation angles, the widths between the double-tooth rings, and the gaps between the cavity and the waveguide, we identified an optimal novel refractive index sensor structure that boasts the best performance indices. Finally, the DTR cavity sensor achieved a sensitivity of 4137 nm/RIU and Figure of merit (FOM) of 59.1. Given the high complexity and sensitivity of the overall structure, this nanoscale refractive index sensor can be applied to the detection of oil concentration in industrial oil–water mixtures, yielding highly precise results.

Keywords: Fano resonance; plasmonic-waveguide coupling systems; MIM; refractive index sensor



Citation: Li, L.; Yan, S.; Cui, Y.; Zhu, C.; Wu, T.; Zhang, Q.; Gao, G. Nano Application of Oil Concentration Detection Using Double-Tooth Ring Plasma Sensing. *Appl. Nano* **2024**, *5*, 20–32. <https://doi.org/10.3390/applnano5010003>

Academic Editor: Angelo Maria Taglietti

Received: 3 January 2024

Revised: 8 February 2024

Accepted: 13 February 2024

Published: 23 February 2024



Copyright: © 2024 by the authors. Licensee MDPI, Basel, Switzerland. This article is an open access article distributed under the terms and conditions of the Creative Commons Attribution (CC BY) license (<https://creativecommons.org/licenses/by/4.0/>).

1. Introduction

Surface plasmon polaritons (SPPs) represent a unique class of electromagnetic waves, arising from the interaction between the free electrons excited by light on a metal surface and photons within a dielectric medium [1]. Their behavior is influenced by specific conditions such as the frequency, angle of incidence, and polarization direction of the incoming light, aligning with the vibrational modes of the surface plasmons on the metal. Both the propagation speed and wavelength of SPPs are contingent upon the characteristics of the metal surface and the refractive index of the medium. SPPs exhibit sub-wavelength scale propagation properties, localized field enhancement effects, and sensitivity around the metal surface, making them extensively applicable in the realm of optical detection [2,3].

The localized field enhancement effects of SPPs serve to amplify spectroscopic phenomena such as Raman scattering and fluorescence. Furthermore, as SPPs propagate along a metal surface, they experience attenuation in the direction of light propagation. This positions SPPs as an exceptionally sensitive tool for sensing applications. For instance, they are employed in surface enhanced Raman scattering (SERS) for the high-sensitivity detection of molecules, as well as in surface plasmon resonance sensors, microscopy imaging, and photonic devices [4]. Additionally, they hold potential utility in photovoltaic technologies, capable of enhancing the efficiency of solar cells. These applications leverage the unique characteristics and effects of SPPs, unveiling new possibilities for research and application across various domains [5].

In recent years, metal–insulator–metal (MIM) waveguide structures have demonstrated the capability to confine and guide surface plasmon polaritons (SPPs), enabling the effective localization of light fields between the metal surface and the insulator [6,7]. This facilitates the enhancement of electromagnetic fields on the metal surface, thereby promoting the generation of SPPs. The metal in these structures provides free electrons to support the propagation of SPPs, while the insulator prevents energy leakage of SPPs into the surrounding medium, achieving efficient transmission of SPPs [8].

The structural parameters of MIM waveguides significantly influence the propagation characteristics of SPPs, such as the type of metal, the refractive index of the insulator, and the dimensions of the waveguide [9]. By adjusting these parameters, one can control and tune the propagation speed, wavelength, and transmission losses of SPPs. Therefore, this structure, capitalizing on the interactions among the metal, insulator, and their interface, serves as a key direction for optimizing nano-scale sensor structures. It enables the effective manipulation and application of SPPs [10].

For example, Rashid et al. proposed a refractive index sensor based on the coupling of three circular rings, achieving a maximum sensitivity of 3573.3 nm/RIU with Figure of merit (FOM) of 21.9 [11]. Kazanskiy et al. introduced a semi-circular resonator loaded with periodically decorated nano-dots, achieving an optimal sensitivity of 1084.21 nm/RIU [12].

Wang et al. presented a circular open-ring resonator structure, with a maximum sensitivity of 1114.3 nm/RIU and Figure of merit (FOM) of 55.71 [13]. Khani and Hayati designed elliptical resonators with sensitivities up to values of up to 550 nm per refractive index unit, with a high FOM value of 282.5 RIU⁻¹ near the resonance wavelength of 592 nm [14]. Rakhshani analyzed a compact refractive index sensor in 2-D plasmonic waveguide by hexagonal-ring cavity. The temperature sensitivity values were up to 4270 nm/refractive index unit (RIU) and 0.56 nm/°C, respectively [15].

“nm/RIU” stands for nanometers per refractive index unit. This unit represents the amount of wavelength change in nanometers corresponding to a change in refractive index unit. It is used to indicate the resolution and sensitivity of optical sensors in detecting changes in the refractive index of a medium.

In plasmonic-waveguide coupling systems, a variety of optical phenomena can be observed, such as dispersion effects, Fano resonances, surface plasmon resonances, and more. Fano resonance plays a crucial role in these plasmonic-waveguide coupling systems. Near the surface of a metal, free electrons oscillate under the excitation of incident light, forming plasmonic vibrations [16]. Fano resonance is a result of the interaction between these plasmonic vibrations and waveguide modes. When their wavelengths match those of the waveguide modes, intense coupling occurs, leading to the emergence of Fano resonance. When a continuous background scattering spectrum overlaps with a discrete spectral line, Fano resonance appears.

Bright mode and dark mode are two modes related to the phenomenon of optical resonance, which together form the Fano resonance. The bright mode is the main optical mode contributing to the Fano resonance and is characterized by the formation of distinct peaks in the spectral lines. When propagating and transmitted waves are in phase and superimposed, they are coherently enhanced at specific wavelengths, forming a peak; the bright mode. The bright mode is usually represented by a peak in the Fano resonance spectral line, indicating a significant increase in light intensity at this wavelength. The dark mode is another optical mode in the Fano resonance and is characterized by the formation of a valley or trough in the Fano resonance spectral line [17,18].

Dark mode corresponds to a situation where the propagating and transmitting waves are in opposite phase or out of phase in the optical structure. When propagating and transmitting waves are phase-opposed and out of phase, they coherently cancel out at a specific wavelength, forming a valley; the dark mode. The dark mode usually manifests itself as a trough in the Fano resonance spectral line, indicating a significant reduction in light intensity at this wavelength. The combination of these two modes gives the Fano

resonance a flexible tuning property in different applications and can be used in optical applications such as sensing, filtering, and modulation [19,20].

In this study, based on the properties of optical Fano resonances and the plasmonic-waveguide coupling system, we propose a novel nano-scale refractive index sensor structure comprising an MIM waveguide and a DTR cavity. We employed the finite element method (FEM) and coupled-mode theory to comprehensively evaluate the propagation characteristics of the entire structure, both of which can analyze the propagation and coupling of waveguide modes.

The simulation results indicated that the presence of a rectangular stub introduces non-uniformity in the transverse dimensions of the waveguide. This non-uniformity can alter the propagation path and mode distribution of electromagnetic waves in the waveguide, resulting in broadband characteristics in the frequency domain. Double-tooth ring and metal waveguide coupling structures are designed to produce a narrow band in the frequency domain by virtue of their unique geometry and material parameters. This means that only light waves in a specific frequency range can be effectively propagated and coupled. Due to the overlap in frequency between continuous broadband modes and discrete narrowband modes, this interference results in asymmetric waveform characteristics, leading to an asymmetric Fano resonance waveform.

We studied the influence of variations in refractive index and structural geometric parameters on the transmission characteristics, including the rotation angles, the width between the double-tooth rings, and the gap between the DTR cavity and the waveguide. The results showed that different geometric parameters have varied impacts on the transmission curve, the bandwidth of the system, and the performance indicators of the system. Moreover, based on the optimized structural parameters identified, the maximum sensitivity and Figure of merit (FOM) coefficient obtained demonstrate excellent sensitivity and refractive effects for oil concentration detection in industrial oil–water mixtures.

2. Materials and Methods

Figure 1 is a plan view of the entire coupled cavity and the composition of the dielectric material. The coupling structure consisted of an MIM waveguide and DTR cavity. As shown in Figure 1, the green portion utilizes silver metal material as the substrate because it can effectively conduct electromagnetic waves, has low optical losses, and reduces energy loss. The white portion represents the air medium. The relative permittivity of air is ϵ_d , and the relative permittivity of metallic silver is defined as follows [21,22]:

$$\epsilon(\omega) = \epsilon_\infty + \frac{\epsilon_s - \epsilon_\infty}{1 + i\tau\omega} + \frac{\sigma}{i\omega\epsilon_0} \quad (1)$$

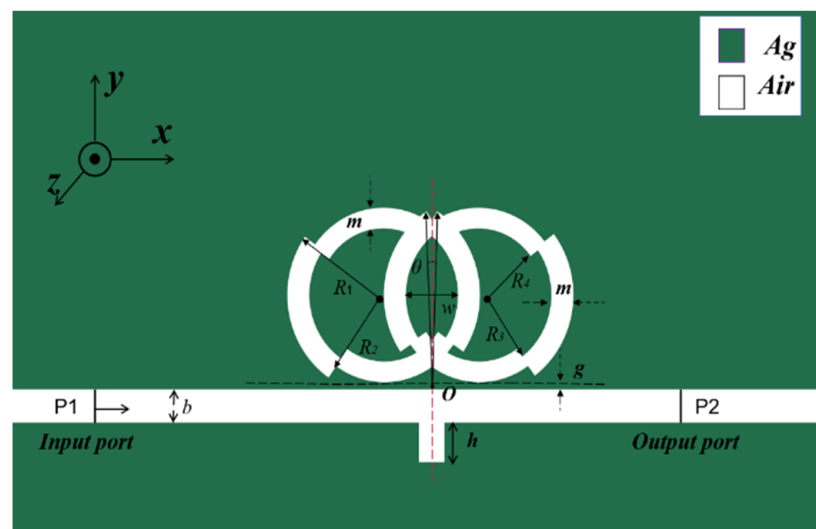


Figure 1. Two-dimensional plan of the overall structure.

In the equation, the explanation of parameter values is infinite frequency relative permittivity $\epsilon_\infty = 3.8344$, static dielectric strength $\epsilon_s = -9530.5$, slack time $\tau = 7.4 \times 10^{-15}$ s, and electrical conductivity $\sigma = 1.1486 \times 10^7$ s/m.

Since the material properties are homogeneous in all three dimensions, three-dimensional effects have almost no impact on the magnetic field distribution. Therefore, we can use a two-dimensional model to approximate the magnetic field characteristics of a three-dimensional structure (Table 1). This simplification method significantly reduces computational complexity and yields results very close to the actual three-dimensional situation, enabling a better study and understanding of the magnetic field behavior of materials [23,24].

Table 1. Definition of the geometric parameters of the model.

Parameter	Definition
R_1, R_2, R_3, R_4	Different radius of tooth ring outer circle
θ	Angle of rotation of double-tooth rings
w	Width between the double-tooth rings
g	Gap between the cavity and the waveguide
b	Breadth of the MIM waveguide
h	Height of rectangular stub
m	Thickness of the dielectric layer of the Double-tooth Rings
O	The center point
P1	Input ports
P2	Output ports

Meanwhile, the MIM waveguide can enable the propagation of SPPs by introducing an insulating layer between two metal layers. Because odd symmetric modes experience strong coupling and attenuation in the insulating layer, resulting in higher energy losses and shorter propagation distances [25–27]. In contrast, even symmetry modes exhibit longer propagation distances and lower energy losses. Therefore, to ensure that only one even symmetry mode can propagate and effectively enhance the transmission efficiency of even symmetry modes while reducing energy losses, selecting an insulator layer thickness of 50 nm met the requirements [28].

The SPPs on the surface of the metal layer are excited by the transverse magnetic mode (TM), and the formula of the transverse magnetic mode is as follows [29]:

$$\tan(kw) = -\frac{2k\alpha_c}{k^2 + p^2\alpha_c} \quad (2)$$

From this formula, k is the wave vector, and p is the ratio of the dielectric constant ϵ_{in} to the metal dielectric constant ϵ_m , $\alpha_c = [k_0^2(\epsilon_{in} - \epsilon_m) + k]^{\frac{1}{2}}$.

The characteristics of the sensor, in this structure, are assessed by three parameters: FWHM, sensitivity, and Figure of merit (FOM) [30]. FWHM refers to the two points on the spectrum line where the energy reaches half of the peak value, and the distance between these two points represents the width of the spectrum line, that is, the sharpness of the spectrum line. Figure of merit (FOM) is an index used to assess and compare the performance of different systems or components. It is a weighted combination of multiple parameters which represent the key performance of the system or component. The relationship can be represented by the following formula [31,32]:

$$S = \frac{\Delta\lambda}{\Delta n} \quad (3)$$

$$FOM = \frac{S}{FWHM} \quad (4)$$

where the refractive index changes by Δn , and the wavelength changes by $\Delta\lambda$. After confirming the above required conditions, the geometrical model of the coupling structure

of the sensor was built using COMSOL Multiphysics 5.4a (COMSOL Inc., Stockholm, Sweden), and ultra-fine triangles were selected to mesh-segment the waveguide coupling structure region. The wavelength range of 2500–3600 nm with a step size of 1 nm was set after preliminary simulation.

3. Simulation Results and Analysis

To begin with, the initial structural parameters of the sensor were set as follows: $R_1 = 210$ nm, $R_2 = 185$ nm, $R_3 = 160$ nm, $R_4 = 135$ nm, $m = 50$ nm, $h = 100$ nm, $w = 100$ nm, and $g = 10$ nm.

As depicted in Figure 2, the black line, red line, and blue line, respectively, represent the transmission spectra of the single rectangular stub, all system, and the single DTR. The wavelength range was from 2500 nm to 3300 nm.

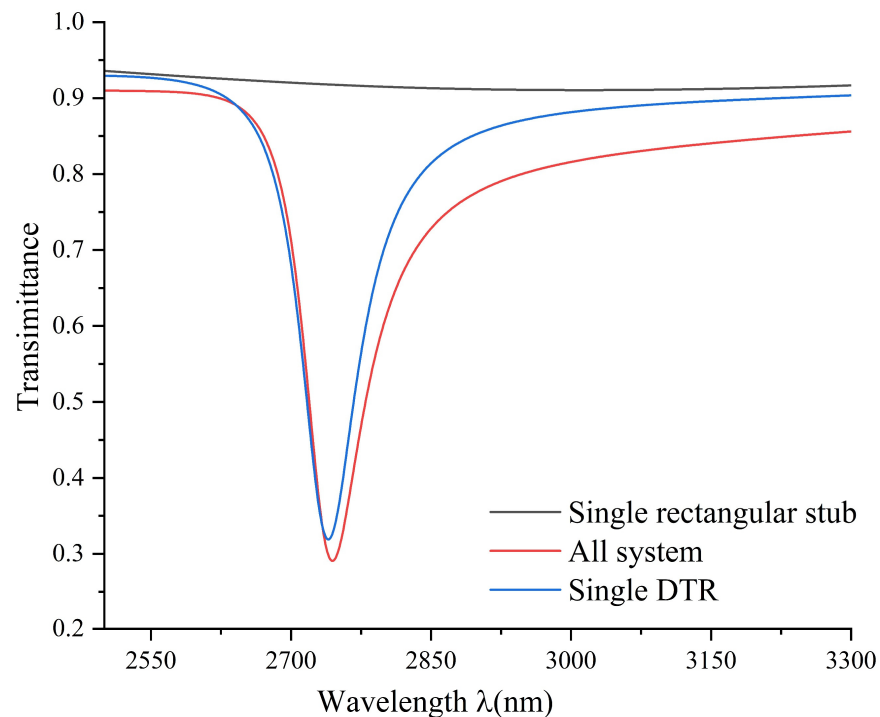


Figure 2. Transmission spectra of the single rectangular stub (black line), all system (red line), and the single DTR structure (blue line).

The transmission spectrum of a single rectangular stub had a slightly upward-sloping straight line, with light signals at most frequencies exhibiting high transmissivity, featuring continuous broadband transmission characteristics. Through transmission spectrum analysis, when the refractive index of the two structures was constant, the cavity corresponded to a very narrow range of wavelengths, manifesting as sharp peaks and presenting Fano resonance phenomenon.

In order to better study the impact of the rectangular stub on Fano resonance, we investigated the sensing performance of an all system that consisted of the double-tooth ring structure with the rectangular stub, and the single TDR structure that did not couple the rectangular stub. As shown in Figure 3, it can be observed that in both structures, SPPs can traverse the waveguide and couple into the cavity, undergoing significant resonance, and the magnetic field distributions were similar. Therefore, the introduction of the rectangular stub reduced the propagation of SPPs in the waveguide, generated stronger resonance, and promoted the occurrence of Fano resonance.

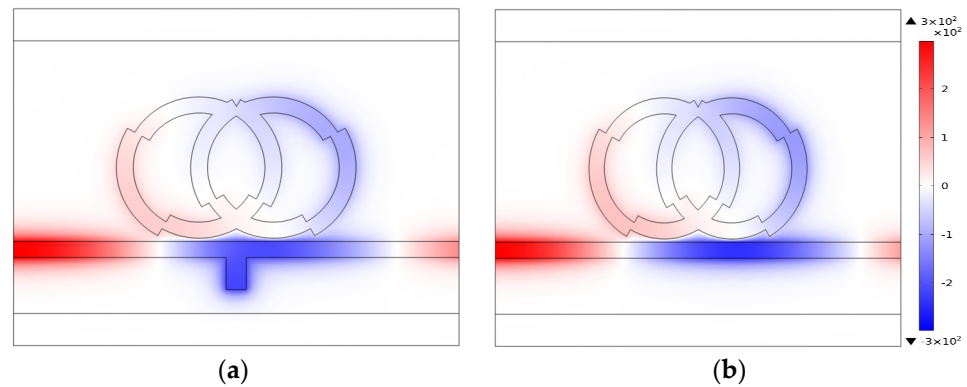


Figure 3. Magnetic field distributions at $n = 1.00$ of (a) the whole structure. (b) The single DTR structure without a rectangular stub.

For the effect of different geometrical parameters on the nano refractive index sensor, the different angles of the TDR were first analyzed.

The initial structural parameters remained fixed. In order to study the effect of angle on the Fano resonance in depth, we compared the transmission spectra at different angles. The θ values were set to 0° , 30° , 60° , 90° , 120° , 150° , and 180° . As shown in the transmission spectra in Figure 4, the structure at $\theta = 120^\circ$ achieved a curve with high transmissivity, and the magnetic field strength of the coupled cavity was extremely low, indicating that this sensor had very poor light-limiting capability. When $\theta = 0^\circ$ (180°), the structure produced an ultra-low transmissivity, with an asymmetrical curve at larger wavelengths, demonstrating that Fano resonance exhibited high sensitivity. Meanwhile, from its transmission curve, it is known that $\theta = 0^\circ$ (180°) had a low trough, which had a better light-limiting ability.

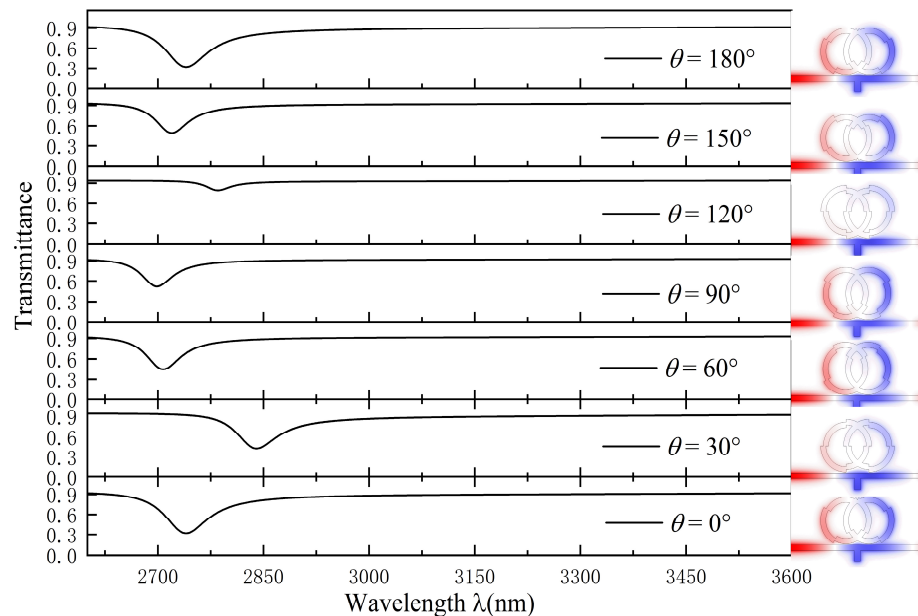


Figure 4. Transmission spectra of the different angles.

As a nanoscale refractive index sensor, this property is very important to enable good stability during the detection process. The other angles produced transmission spectral lines, which all showed higher transmittance, inconsistent wavelengths, and poor propagation characteristics relative to those at 0° will not be analyzed one by one. In summary, the performance of the sensor varied significantly with the change in the rotation angle of the DTR. $\theta = 0^\circ$ (180°) was the optimal rotation angle for the structure.

Subsequently, the impact of the width between the double-tooth rings on the sensor's performance was studied. Keeping the initial structural parameters were unchanged, the w was varied in steps of 10 nm, ranging from 80 nm to 120 nm. The results are shown in Figure 5, from which it can be observed that as the width increases, the wavelength increases, and the waveform of the transmission spectrum shifts approximately equidistantly to the right; the FWHM width of the transmission curve of the transmission spectrum becomes larger. The sensitivity linear fitting for different slit widths is shown in Figure 5b.

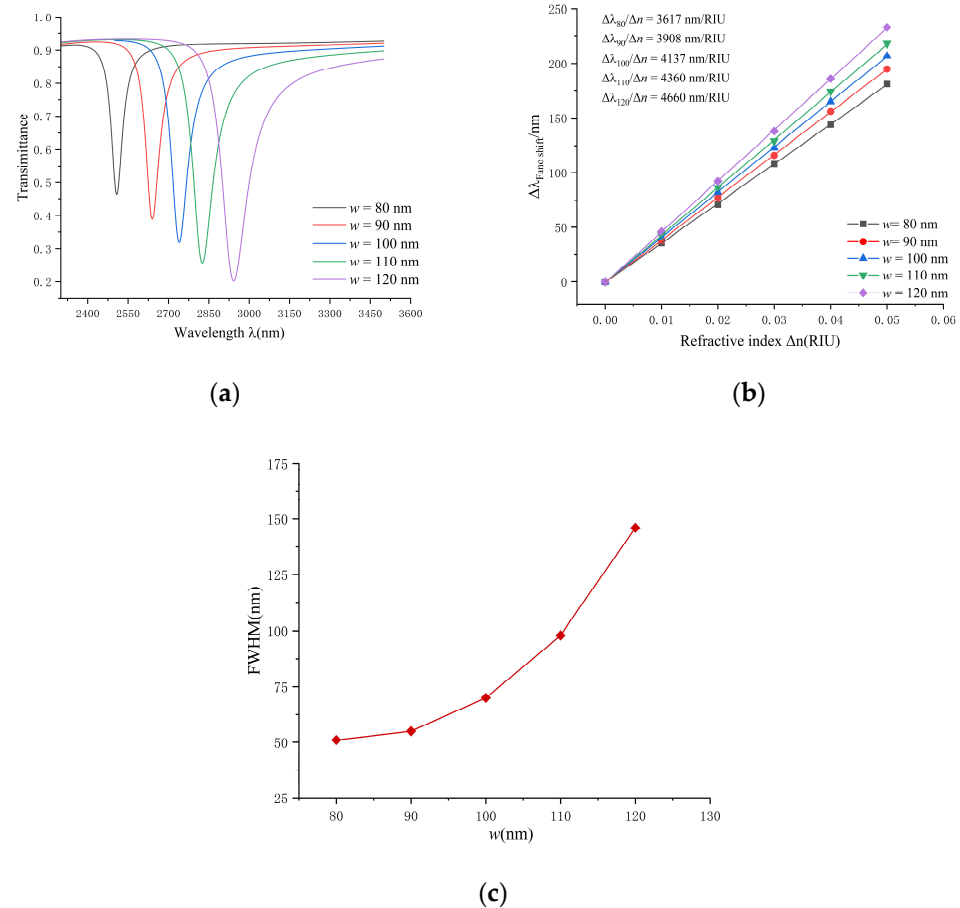


Figure 5. (a) Transmission spectra for the different widths between the double-tooth rings. (b) Fitting lines of sensitivity at the diverse widths between the double-tooth rings. (c) Changes of FWHM values at the various widths between the double-tooth rings.

When the width increased, the overall system sensitivity increased. By calculating Figure of merit (FOM) using the formula, its FOM values were in the range of 70.9, 72.4, 59.1, 44.5, and 31.9; however, the structures of 80 nm and 90 nm were not selected for further discussion because highly optimized sensors may be more sensitive to changes in the environment or to rapid changes in the target substance, and the transmission curves have high troughs, which may result in shorter response times. In some applications, a long response time may be more appropriate, so we chose the $w = 100$ nm condition to achieve a longer response time.

Based on the above discussion, we chose the width of 100 nm and the other geometric parameters remained invariant. Then, we examined the impact of the height of the rectangular stub in the coupled structure on the transmission characteristics. The height values of the rectangular stub were set to 80 nm, 90 nm, 100 nm, 110 nm, and 120 nm.

As shown in Figure 6, the dip position of the Fano resonance remained basically constant as the height of the rectangular stub increased. The shape of the Fano resonance curve shows an asymmetric shape, and the degree of asymmetry gradually becomes larger.

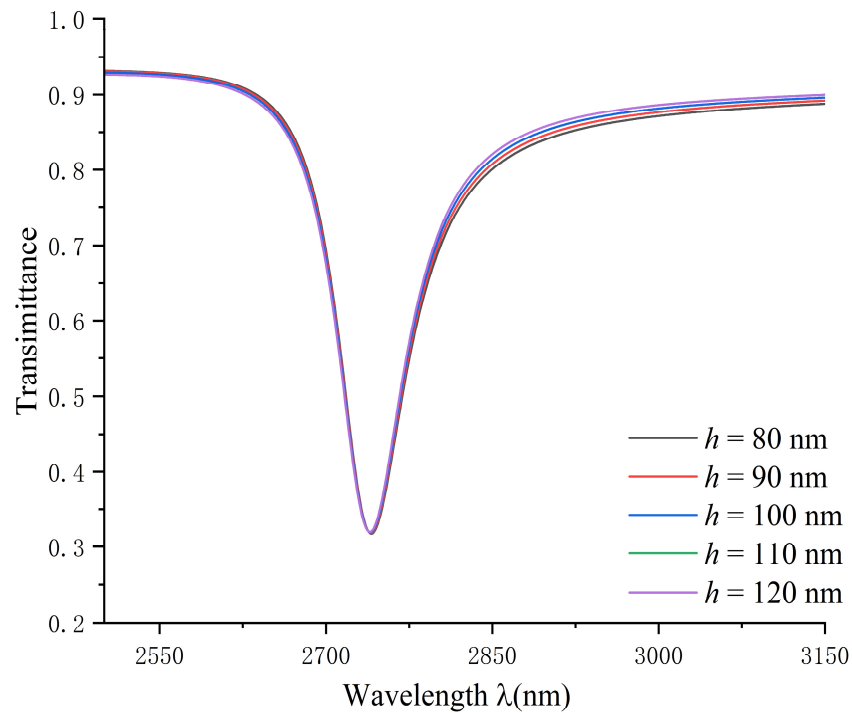


Figure 6. Transmission spectra for the different heights of rectangular stub.

In conclusion, in Fano resonance, the MIM waveguide has been designed by introducing a rectangular stub structure capable of triggering the resonance in the interface between the metal layer and the insulator layer. This structure results in the amplification and localization of propagating electromagnetic waves within a specific frequency range, giving the MIM waveguide a continuous broadband profile. The continuous broadband state affects the line profile (peak height and shape) of the Fano resonance, causing variations in the amplitude and shape of the propagating wave, but not on the wavelength of the dip (the wavelength of propagation in the waveguide).

Following this, the impact of the coupling gap between the waveguide structure and the DTR structure on the sensing characteristics was assessed.

The initial structural parameters were unchanged, and the coupling gap varied within the range of 5 nm to 25 nm, with a step size of 5 nm. The transmission characteristics curves for different values are shown in Figure 7. As the coupling gap got larger, the wavelength became smaller, resulting in a blue shift of the transmission wavelength; the FWHM decreased, the transmittance increased, the coupling strength weakened, and the resonance diminished.

The sensitivity decreased as the coupling gap increased. At $g = 5$ nm, the sensitivity reached 4600 nm/RIU, and at $g = 25$ nm, it was reduced to 3851 nm/RIU. When $g < 10$ nm, the FWHM line chart showed a very steep trend, resulting in a relatively small Figure of merit (FOM) value for the coupling structure at $g = 5$ nm. When g is less than or equal to zero, it effectively means that there is no gap, and the two structures are in direct contact. In this case, coupling effects can become very strong and may lead to highly non-linear behavior. This may include extremely large transmittances, very narrow FWHM, and highly sensitive sensing properties. So, the coupling gap at $g = 10$ nm was chosen to obtain the best sensing performance with low transmittance and at the same time the best sensing performance of the whole system.

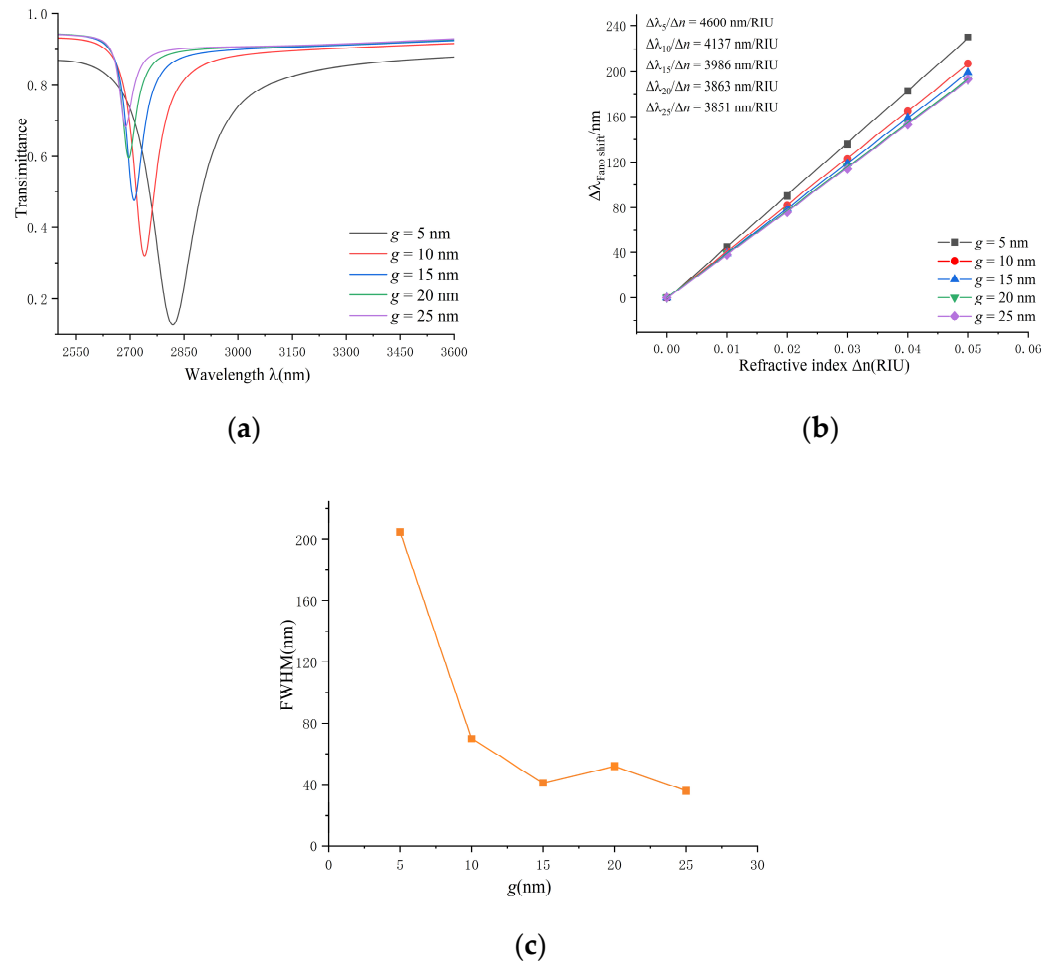


Figure 7. (a) Transmission spectra of various coupling gaps. (b) Fitting lines of sensitivity at diverse coupling gaps. (c) Changes of FWHM values at different coupling distances.

Finally, we analyzed the refractive index. The initial value of refractive index was $n = 1.00$, the step size was 0.01, and ends when the refractive index was $n = 1.05$. The results are shown in Figure 8.

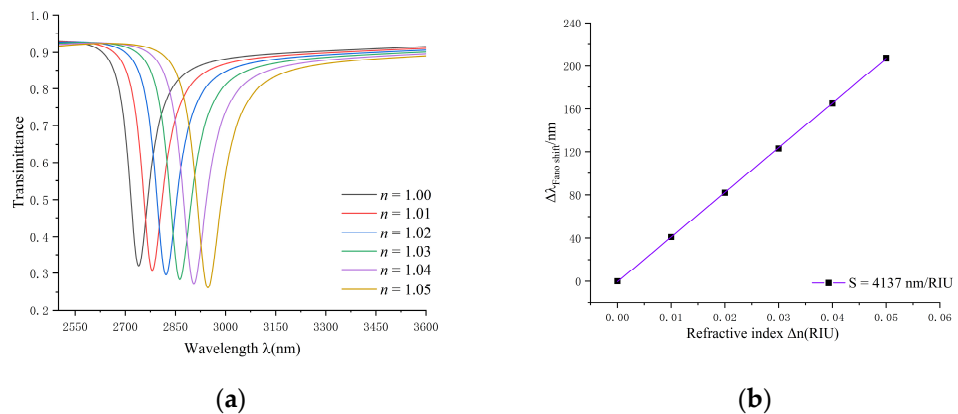


Figure 8. (a) Transmission spectra of diverse refractive indices. (b) Fitting lines of dip wavelength change with refractive index variation.

As the refractive index progressively increased, the corresponding wavelength also increased, leading to a noticeable redshift in the transmitted spectrum. The waveform of the transmission spectrum remained unaffected by changes in the refractive index. The

wavelength differences between various peaks were the same, with wavelengths shifting equidistantly. Through linear fitting, the sensitivity of the DTR refractive index sensor was determined to be 4137 nm/RIU, with an optimal value of 59.1, representing the optimum parameters for this coupling structure (Table 2).

Table 2. Comparison with other literature data.

Structure Type	Sensitivity (nm/RIU)	Figure of Merit (FOM)	Operating Wavelength Range
Three circular rings cavity [11]	3573.3	21.9	1400 < λ < 3000
NDs decorated semi-ring cavity [12]	1084.21	57.06	800 < λ < 1200
A circular split-ring resonator cavity [13]	1114.3	55.71	750 < λ < 1350
DTR cavity	4137	59.1	2500 < λ < 3600

To select the optimal performance index to ensure that the device can perform as expected, the effect of the refractive index change on the transmission spectrum must be carefully considered in the design of the optical device.

4. Application

Due to the sensing characteristics of the DTR structure, it exhibited high sensitivity, complex structure, and ease of miniaturization and integration. It is suitable for application as a sensor to detect oil concentration in industrial processes. The properties of oil–water mixtures depend on the ratio and physical properties of the oil and water. For example, during metal cutting and machining, machinery and equipment may become hot, and an oil–water mixture can serve as a coolant to help reduce the temperature of equipment and prevent overheating. The oil concentration in coolants typically ranges from 5% to 20%. In addition, oil–water mixtures in detergents can be used to remove oil stains, usually at a concentration of 0.1% to 5%. Oil concentrations in food processing can vary from 10% to 100% depending on the type of food and cooking method, and so on.

The mixture refers to oil and water mixed in different proportions and then turned into other solvents through a special process. Such solvents because of the different oil content (water content), will produce a change in the refractive index. In filling to the nano-refractive index sensor, it will be because of the difference of refractive index, which will cause the change of wavelength.

The process of monitoring the oil concentration using this sensor is shown below: the oil–water mixture is used to exhaust the air from the recesses of the sensor. When the nanosensor comes into contact with the oil–water mixture, the air in the groove is expelled, filling the groove with liquid. Since the oil–water mixture has a different concentration, the corresponding refractive index is also different. By monitoring the transmission or reflection of light, the nanosensor generates an image called a Fano resonance curve. As the oil concentration changes, the refractive index of the medium of the oil–water mixture also changes, which can lead to changes in the Fano resonance curve. The nanosensor detects these changes and compares them to a pre-established oil concentration–refractive index relationship.

The relationship between oil concentration and refractive index was found as follows:

$$n = n_0 + k \times c \quad (5)$$

where n is the refractive index of the oil–water mixture, n_0 is the refractive index of the water, k is a constant related to the composition and wavelength of the mixture, and c is the concentration of the oil in the mixture.

Monitoring of the oil concentration was carried out at 20 °C with a constant k of 0.04 and n_0 of 1.333. The oil concentration was taken as 0%, 20%, 40%, 60%, 80%, and 100%. The refractive index of the oil–water mixture was calculated as 1.333, 1.339, 1.345, 1.351, 1.357, and 1.363.

The sensitivity S_c of the concentration sensor can be given by the following equation:

$$S_c = \frac{\Delta\lambda}{\Delta c} \quad (6)$$

In this equation, $\Delta\lambda$ represents the translation of the transmission spectrum and Δc represents the concentration change.

The transmission curve and sensitivity are shown in Figure 9. The transmittance of the sensor was too large in the second trough, so it was analyzed with the first wave trough. As the concentration of the oil became larger, the position of the trough moved from 2325 nm to 2397 nm, the curve shifted approximately equidistant to the right, and the transmittance curve showed an obvious red shift. Modern optical instruments can be accurate down to the nanometer scale and can accurately detect wavelengths. The linear fit line for the sensitivity of the sensor is shown in Figure 9b, and the sensitivity of the concentration sensor was calculated to be 71.5 in order to ensure the accuracy of the measurement.

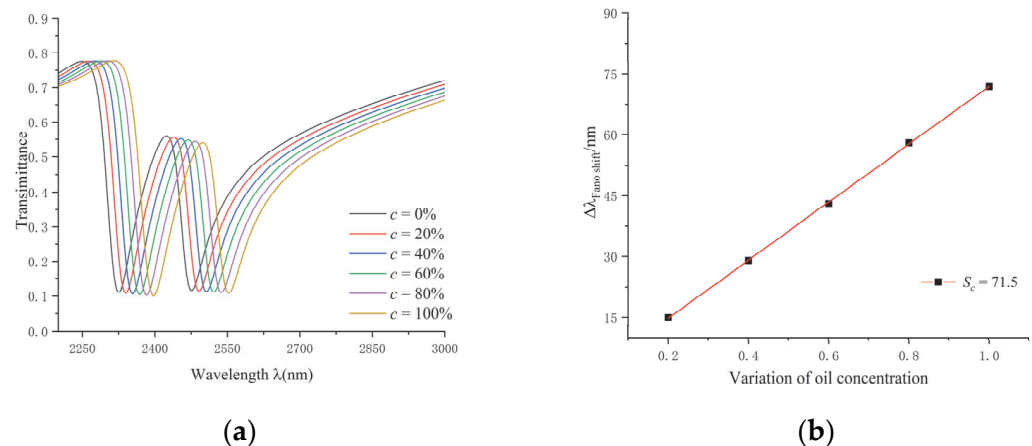


Figure 9. (a) Transmission spectra at gradually increasing oil concentrations. (b) Sensitivity fitting line for concentration sensors.

5. Conclusions

Based on the unique characteristics of optical Fano resonance and the plasma-waveguide coupling system, we designed a nanoscale refractive index sensor. It consists of the MIM waveguide and the DTR.

Due to the influence of distinct geometrical parameters on the sensing characteristics, which include the rotation angles, the widths of the double-tooth ring, and the gaps between the cavity and the waveguide, the analysis focused on the introduction of a rectangular stub. The analysis obtained that the continuous broadband mode and discrete narrowband mode had an overlapping area in frequency, and this interference creates an asymmetric feature of the waveform. Secondly, the rotation angles of the DTR were compared and the finest angle was selected. At last, by consolidating the optimal structural parameters, a novel sensor structure was achieved. The sensitivity of this DTR cavity was 4137 nm/RIU with Figure of merit (FOM) of 59.1.

The designed sensor can be applied industrially with the best performance. Accordingly, the application of the concentration sensor for monitoring oil concentration in industrial oil–water mixtures was presented. The data showed that this oil concentration sensor had a sensitivity of 71.5 and has a promising application.

Author Contributions: Conceptualization, S.Y. and L.L.; methodology, L.L.; software, Y.C.; validation, S.Y. and C.Z.; formal analysis, L.L.; investigation, L.L.; resources, T.W.; data curation, L.L.; writing—original draft preparation, L.L.; writing—review and editing, Q.Z.; visualization, G.G.; supervision, S.Y.; project administration and funding acquisition, S.Y. All authors have read and agreed to the published version of the manuscript.

Funding: The work was supported in part by the National Natural Science Foundation of China under Grant No. 62374148, 62003315 and Grant No. 61975189, in part by the Zhejiang Provincial Natural Science Foundation of China under Grant No. LD21F050001, the Key Research Project by Department of Water Resources of Zhejiang Province under Grant No. RA2101, the Key Research and Development Project of Zhejiang Province under Grant No. 2021C03019, and the Scientific research foundation of Zhejiang University of Water Resources and Electric Power under Grant No. xky2022032.

Data Availability Statement: The data provided in this study are available upon request from the corresponding author.

Acknowledgments: The authors are grateful to other colleagues in the laboratory for their understanding and help. They also thank the affiliates for providing the research platform and the sponsors for financial support.

Conflicts of Interest: The authors declare no conflict of interest.

References

1. Rawashdeh, A.; Wildenborg, A.; Liu, E.; Gao, Z.; Czaplewski, D.A.; Qu, H.; Suh, J.Y.; Yang, A. High-quality surface plasmon polaritons in large-area sodium nanostructures. *Nano Lett.* **2023**, *23*, 469–475. [[CrossRef](#)]
2. Pommier, D.; Hufschmitt, Z.; Zhang, C.; Lai, Y.; Dujardin, G.; Le Moal, E.; Sauvan, C.; Greffet, J.-J.; Wang, J.; Boer-Duchemin, E. Nanoscale Electrical Excitation of Surface Plasmon Polaritons with a Nanoantenna Tunneling Junction. *ACS Photonics* **2023**, *10*, 2641–2649. [[CrossRef](#)]
3. Han, X.X.; Rodriguez, R.S.; Haynes, C.L.; Ozaki, Y.; Zhao, B. Surface-enhanced Raman spectroscopy. *Nat. Rev. Methods Primers* **2021**, *1*, 87. [[CrossRef](#)]
4. Terekhin, P.N.; Benhayoun, O.; Weber, S.; Ivanov, D.; Garcia, M.; Rethfeld, B. Influence of surface plasmon polaritons on laser energy absorption and structuring of surface. *Appl. Surf. Sci.* **2020**, *512*, 144420. [[CrossRef](#)]
5. Bell, S.E.J.; Charron, G.; Cortés, E.; Kneipp, J.; De La Chapelle, M.L.; Langer, J.; Procházka, M.; Tran, V.; Schlücker, S. Towards reliable and quantitative surface-enhanced Raman scattering (SERS): From key parameters to good analytical practice. *Angew. Chem. Int. Ed.* **2020**, *59*, 5454–5462. [[CrossRef](#)]
6. Butt, M.A.; Kazanskiy, N.L.; Khonina, S.N. Metal-Insulator-Metal Waveguide Plasmonic Sensor System for Refractive Index Sensing Applications. *Adv. Photonics Res.* **2023**, *4*, 2300079. [[CrossRef](#)]
7. Kazanskiy, N.L.; Khonina, S.N.; Butt, M.A. Plasmonic sensors based on Metal-insulator-metal waveguides for refractive index sensing applications: A brief review. *Phys. E Low Dimens. Syst. Nanostructures* **2020**, *117*, 113798. [[CrossRef](#)]
8. Chou Chau, Y.F.; Chou Chao, C.T.; Huang, H.J.; Kumara, N.T.R.N.; Lim, C.M.; Chiang, H.P. Ultra-high refractive index sensing structure based on a metal-insulator-metal waveguide-coupled T-shape cavity with metal nanorod defects. *Nanomaterials* **2019**, *9*, 1433. [[CrossRef](#)] [[PubMed](#)]
9. Blau, Y.; Gilad, T.; Hanein, Y.; Boag, A.; Scheuer, J. High efficiency coupling to metal-insulator-metal plasmonic waveguides. *Opt. Express* **2022**, *30*, 13757–13764. [[CrossRef](#)] [[PubMed](#)]
10. Tan, Y.M.; Chao, C.-T.C.; Kooh, M.R.R.; Huang, H.J.; Thotagamuge, R.; Lim, C.M.; Chiang, H.-P.; Chau, Y.-F.C. Mid infrared sensing structure based on a metal-insulator-metal waveguides with a triangular-shaped resonator. *Opt. Commun.* **2022**, *516*, 128282. [[CrossRef](#)]
11. Rashid, K.S.; Hassan, F.; Yaseer, A.A.; Tathfif, I.; Sagor, R.H. Gas-sensing and label-free detection of biomaterials employing multiple rings structured plasmonic nanosensor. *Sens. Bio Sens. Res.* **2021**, *33*, 100440. [[CrossRef](#)]
12. Kazanskiy, N.L.; Butt, M.A.; Khonina, S.N. Nanodots decorated MIM semi-ring resonator cavity for biochemical sensing applications. *Photonics Nanostruct.—Fundam. Appl.* **2020**, *42*, 100836. [[CrossRef](#)]
13. Wang, M.; Zhang, M.; Wang, Y. Fano Resonance in an Asymmetric MIM Waveguide Structure and Its Application in a Refractive Index Nanosensor. *Sensors* **2019**, *19*, 791. [[CrossRef](#)]
14. Khani, S.; Hayati, M. An ultra-high sensitive plasmonic refractive index sensor using an elliptical resonator and MIM waveguide. *Superlattices Microstruct.* **2021**, *156*, 106970. [[CrossRef](#)]
15. Rakhshani, M.R.; Mansouri-Birjandi, M.A. High-sensitivity plasmonic sensor based on metal-insulator-metal waveguide and hexagonal-ring cavity. *IEEE Sens. J.* **2016**, *16*, 3041–3046. [[CrossRef](#)]
16. Chao, C.T.C.; Chau, Y.F.C.; Chiang, H.P. Multiple Fano resonance modes in an ultra-compact plasmonic waveguide-cavity system for sensing applications. *Results Phys.* **2021**, *27*, 104527. [[CrossRef](#)]
17. Wahsheh, R.A. Mode coupling enhancement from dielectric to plasmonic waveguides. *Opt. Eng.* **2020**, *59*, 107101.

18. Paul, S.; Ray, M. Multispectral switching using Fano resonance and plasmon-induced transparency in a plasmonic waveguide-coupled resonator system. *Plasmonics* **2019**, *14*, 1113–1122. [[CrossRef](#)]
19. Ravindran, N.; Kumar, S.; Yashini, M.; Rajeshwari, S.; Mamatchi, C.A.; Thirunavookarasu, S.; Sunil, C.K. Recent advances in Surface Plasmon Resonance (SPR) biosensors for food analysis: A review. *Crit. Rev. Food Sci. Nutr.* **2023**, *63*, 1055–1077. [[CrossRef](#)]
20. Yesudasu, V.; Pradhan, H.S.; Pandya, R.J. Recent progress in surface plasmon resonance based sensors: A comprehensive review. *Heliyon* **2021**, *7*, e06321. [[CrossRef](#)]
21. Stone, J.M.; Hawley, J.F.; Gammie, C.F.; Balbus, S.A. Three-dimensional magnetohydrodynamical simulations of vertically stratified accretion disks. *Astrophys. J.* **1996**, *463*, 656. [[CrossRef](#)]
22. Gai, H.; Wang, J.; Tian, Q. Modified Debye model parameters of metals applicable for broadband calculations. *Appl. Opt.* **2007**, *46*, 2229–2233. [[CrossRef](#)] [[PubMed](#)]
23. Yang, Z.; Wang, J.; Shao, Y.; Jin, Y.; Yi, M. Studying corrosion of silver thin film by surface plasmon resonance technique. *Opt. Quantum Electron.* **2020**, *52*, 1–8. [[CrossRef](#)]
24. Zhang, C.; Ji, C.; Park, Y.B.; Guo, L.J. Thin-Metal-Film-Based Transparent Conductors: Material Preparation, Optical Design, and Device Applications. *Adv. Opt. Mater.* **2021**, *9*, 2001298. [[CrossRef](#)]
25. Liu, L.; Luo, Y.; Zhao, Z.; Zhang, W.; Gao, G.; Zeng, B.; Wang, C.; Luo, X. Large area and deep sub-wavelength interference lithography employing odd surface plasmon modes. *Sci. Rep.* **2016**, *6*, 30450. [[CrossRef](#)] [[PubMed](#)]
26. Smith, C.L.C.; Stenger, N.; Kristensen, A.; Mortensen, N.A. Gap and channeled plasmons in tapered grooves: A review. *Nanoscale* **2015**, *7*, 9355–9386. [[CrossRef](#)]
27. Han, Z.; Bozhevolnyi, S.I. Radiation guiding with surface plasmon polaritons. *Rep. Prog. Phys.* **2012**, *76*, 016402. [[CrossRef](#)]
28. Azam, M.; Ghaffar, A.; Jamil, Y.; Bhatti, H.N. Hybrid surface plasmon polariton (SPPs) modes between metal and anisotropic plasma interface. *J. Ovonic Res. Vol.* **2021**, *17*, 509–517. [[CrossRef](#)]
29. Choi, B.B.; Kim, B.; Bice, J.; Taylor, C.; Jiang, P. Inverse DVD-R grating structured SPR sensor platform with high sensitivity and figure of merit. *J. Ind. Eng. Chem.* **2022**, *116*, 321–330. [[CrossRef](#)]
30. Alagdar, M.; Yousif, B.; Areed, N.F.; Elzalabani, M. Improved the quality factor and sensitivity of a surface plasmon resonance sensor with transition metal dichalcogenide 2D nanomaterials. *J. Nanoparticle Res.* **2020**, *22*, 1–13. [[CrossRef](#)]
31. Liu, L.; Liu, Z.; Zhang, Y.; Liu, S. Multi-channel Optical Fiber Surface Plasmon Resonance Sensor with Narrow FWHM, High Figure of Merit, and Wide Detection Range. *Plasmonics* **2022**, *17*, 2235–2244. [[CrossRef](#)]
32. Alagdar, M.; Yousif, B.; Areed, N.F.; Elzalabani, M. Highly sensitive fiber optic surface plasmon resonance sensor employing 2D nanomaterials. *Appl. Phys. A* **2020**, *126*, 1–16. [[CrossRef](#)]

Disclaimer/Publisher’s Note: The statements, opinions and data contained in all publications are solely those of the individual author(s) and contributor(s) and not of MDPI and/or the editor(s). MDPI and/or the editor(s) disclaim responsibility for any injury to people or property resulting from any ideas, methods, instructions or products referred to in the content.